JMEPEG (2010) 19:860–867
DOI: 10.1007/s11665-009-9539-y

1059-9495/$19.00

Dissolution of Eutectic β-$Mg_{17}Al_{12}$ Phase in Magnesium AZ91 Cast Alloy at Temperatures Close to Eutectic Temperature

Tianping Zhu, Zhan W. Chen, and Wei Gao

(Submitted November 30, 2008; in revised form July 30, 2009)

Knowledge on the dissolution kinetics of β_{-eut} phase in cast Mg AZ91 alloy at temperatures close to the eutectic temperature is very useful for various processes of the alloy. In the present study, dissolution of β_{-eut} phase has been investigated experimentally and considered theoretically. Results have confirmed that the kinetics of β_{-eut} dissolution is basically diffusion controlled. Optimum times for dissolution heat treatment practice of different sizes of cast microstructure which are cooling rate dependant during casting could be suggested based on the present calculation. For fusion welding of the alloy, the present results indicate the difficulty of having a heating rate lower than the critical value ("critical heating rate") for a significant reduction of the phase to avoid constitutional liquation.

Keywords constitutional liquation, magnesium alloys, β phase dissolution

1. Introduction

Weight reduction and fuel efficiency in automotive and aerospace industries have resulted in magnesium alloys being used as attractive structural materials. For this reason, there has been a growing demand for magnesium alloys, in particular, a massive growth (~11.5%) in the usage of magnesium alloys for die casting in recent years (Ref 1). AZ91 (Mg-9Al-1Zn) is by far the most popular magnesium die cast alloy. Thus, solidification and the subsequent properties of the cast alloy associated particularly with eutectic β-$Mg_{17}Al_{12}$ (β_{-eut}) phase have been extensively studied (Ref 2-7).

In general, mechanical properties are adversely affected by β_{-eut} phase in cast AZ91 alloy, as fracture often initiates by cracking of β_{-eut} particles (Ref 2, 8). Dissolution treatment eliminates the brittle β_{-eut} phase and hence entails significantly enhanced ductility (Ref 7, 9). Solution treatment for AZ91 alloy has been specified to be at temperature ranging from 413 to 418 °C for 16-24 h (Ref 10). Recent experiments conducted by Yakubtsov et al. (Ref 7) show that at 420 °C 5 h treatment results in dissolution of the majority of β_{-eut} phase. A quantitative prediction of the dissolution kinetics taking into account the size of the as-cast microstructure should be very useful, although it has not been reported.

Tianping Zhu and **Wei Gao**, Department of Chemical & Materials Engineering, University of Auckland, Auckland, New Zealand; and **Zhan W. Chen**, Department of Mechanical & Manufacturing Engineering, AUT University, Auckland, New Zealand. Contact e-mail: tzhu004@aucklanduni.ac.nz.

For many applications, the final assembly often needs parts to be welded together. Hence, there has been an increasing research effort on welding of Mg alloys (Ref 11-18). A major technical problem of welding Mg alloys is the extensive melting in the partially melted zone (PMZ) (Ref 11), which can result in liquation cracking (Ref 19). To avoid liquation cracking in PMZ during welding, β_{-eut} particles must dissolve before T_E (eutectic temperature) is reached. Understanding the dissolution of β_{-eut} phase during heating taking into account the effect of the size of the microstructure is therefore important. If the heating time required for β_{-eut} dissolution during welding was not sufficiently long, pre-welding annealing may then be an approach to minimize liquation cracking during welding. Thus, knowledge on the dissolution kinetics of β_{-eut} phase and a mathematical tool for calculating the dissolution time are required for annealing/homogenization practice.

Considering the importance of the kinetics of β_{-eut} phase dissolution, in the present study, isothermal annealing experiments at two temperatures close to T_E were conducted to determine the dissolution rate of β_{-eut} phase in AZ91 cast alloy. The dissolving process of β_{-eut} phase was then theoretically considered based on diffusion and mass balance during dissolution of a simplified plate-like morphology of β_{-eut} particles. The effect of the as-cast microstructure on the dissolution kinetics of β_{-eut} phase was revealed through the study on cast cooling rate specific samples.

2. Experimental Procedures

A cast plate was made by re-melting commercial AZ91 ingot and pouring into a sand mould with an iron chill at one end and a big riser at the other end of the cast cavity. The design of the mould followed that used for producing a casting plate experiencing increasing cooling rate and hence decreasing grain size toward the chill end by Cáceres et al. (Ref 20). Samples were taken from three locations of the cast plate,

the chill end, the mid-location and the riser end, and used as the starting materials. The microstructures of these location (or cooling rate) specific cast samples are presented in Fig. 1. The samples were further machined into thin specimens with dimensions of $8 \times 8 \times 1.5$ mm^3, and annealed in an electrical furnace for various periods of time. Metallurgical examination was carried out on the broad surface of the thin specimen.

Annealing (dissolution) experiments were conducted at 400 and 420 °C which are above the solvus temperature and close to but below the incipient temperature of constitutional liquation (Ref 17). Annealing of the cast samples was performed in a furnace with protective atmosphere (N_2). The annealed samples were water quenched immediately after removing from the furnace. The standard procedure of metallurgical specimen preparation was followed to mount, grind, polish sample to 1 μm, and etched using 'Acetic-picral' etchant. Microstructure examination was made using both optical microscopy and scanning electron microscopy (SEM). Al concentration was measured using energy dispersive spectroscopy (EDS).

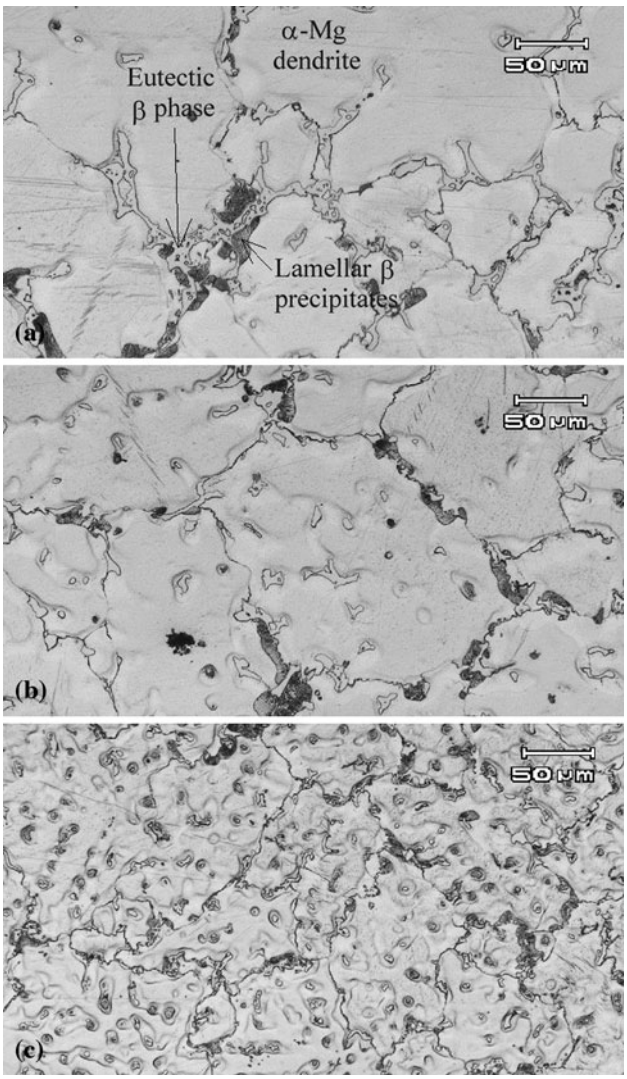

Fig. 1 Micrographs showing the as-cast microstructures in three specific locations of the cast: (a) riser end sample, (b) mid-location sample, and (c) chill end sample

Quantitative analysis of the fraction of β phase (f_β) was conducted using electron back scatter diffraction (EBSD) and normal quantitative analysis on micrographs. EBSD is a technique to evaluate the microstructure of metallic sample through crystallographic analysis. When an electron beam scans on a polycrystalline sample, the crystal structure (or phase) and orientation at each point (grid) is identified. A quantitative result of phase fraction can then be obtained by counting the grids of various phases. EBSD was conducted using FEI Quanta 200F ESEM. EBSD analysis was made only on as-cast samples as a complete EBSD scan takes a long time. Using EBSD for as-cast samples is necessary, as its analytical resolution makes it possible for the quantitative measurement when the fine lamellar precipitates are present.

When cast samples are exposed to the annealing temperature, the local areas of lamellar β (discontinuous precipitates) and α(Mg) with a submicron interlamellar spacing should quickly transform to the stable higher temperature α(Mg). Thus, annealed samples were analyzed using the normal quantitative metallography using "ImageJ" software to quantify the $\beta_{\text{-eut}}$ phase. Digital images taken on the sample etched by "Phospho-picral" etchant shows a strong contrast between the stained α-Mg matrix and the bright $\beta_{\text{-eut}}$ phase. These digital images were transferred into binary (black and white) images, then the fraction of $\beta_{\text{-eut}}$ phase ($f_{\beta\text{-eut}}$) was determined using "ImageJ" software. Three digital images were captured at random locations for each sample in order to achieve a reliable average $f_{\beta\text{-eut}}$.

3. Theoretical Computation

The dissolution process was considered theoretically and the procedure is explained schematically in Fig. 2. The real and more irregular shapes of grains as shown in Fig. 1 have been simplified using hexagonal α(Mg) grains with $\beta_{\text{-eut}}$ particles present in the grain boundaries and also interior (representing those formed within the secondary dendrite branches). In this consideration, we primarily aim to understand the approximate time for the dissolution of $\beta_{\text{-eut}}$ phase affected by the size of microstructure. Hence, we use the following simplified assumptions:

1. $\beta_{\text{-eut}}$ particles have a plate-like morphology, thus 1-D computation could be used; an isolated diffusion field is considered and the overlapping of diffusion field from neighboring $\beta_{\text{-eut}}$ plates has not been taken into account.

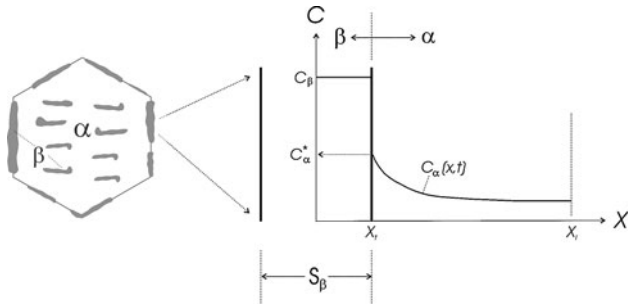

Fig. 2 A schematic illustration of the simplified $\beta_{\text{-eut}}$ present in α(Mg) matrix and compositional distribution. S_β is the thickness of simplified $\beta_{\text{-eut}}$ plate

2. Al diffusivity in α(Mg) matrix is not a function of Al concentration.
3. The effects of Zn and other minor elements on the solid dissolution of $\beta_{\text{-eut}}$ phase can be ignored.
4. β/α interface has been taken as stationary (invariant diffusion field) for the calculation of solute distribution.
5. The dissolution of β phase is in a shape-preserving manner, i.e. the β particle remained in a plate shape through the dissolution process.

Referring to Fig. 2, the mass balance at the moving β/α interface during the dissolution of a $\beta_{\text{-eut}}$ plate can be described by Eq 1, i.e. equalling the flux of Al liberated during the phase transformation β → α (the right-hand side of Eq 1) to the flux of Al diffused into the α(Mg) matrix (the left-hand side of Eq 1).

$$-D_{\text{Al}}\rho_\alpha \frac{dC_\alpha^*}{dx} = \left(C_\beta \rho_\beta - C_\alpha^* \rho_\alpha^*\right)\frac{dX_t}{dt} \quad \text{(Eq 1)}$$

where C_α^* is the Al concentration of α(Mg) phase at β/α interface. ρ_β, ρ_α^*, and ρ_α are the densities of β phase, α(Mg) phase at β/α interface, and average density of α(Mg) phase, respectively. X_t is the location of β/α interface at time t. D_{Al} is the Al diffusivity in α(Mg) phase.

The right-hand side of Eq 1 can be expressed by Eq 2 for locating the moving β/α interface.

$$\frac{dX_t}{dt}\left(C_\beta \rho_\beta - C_\alpha^* \rho_\alpha^*\right) \approx \frac{1}{\Delta t}\left(\int_{X_t}^{X_1} C_\alpha(x,t)\,dx - \int_{X_{t-\Delta t}}^{X_1} C_\alpha(x,t-\Delta t)\,dx\right) \times \rho_\alpha \quad \text{(Eq 2)}$$

where X_1 (see also Fig. 2) is the location of far end boundary of diffusion domain taken approximately as an half of the secondary dendritic arm spacing. As already described, the present casting procedure and die dimension followed that of Cáceres et al. (Ref 21). Grain sizes in the three locations (260, 240, and 200 μm) measured in the present work are almost the same as those measured by Cáceres et al. in the same locations, suggesting that the alloy composition and casting conditions are close to be identical. Cáceres et al. also provided SDAS values measured following a special etching procedure of the metallographic samples. Their SDAS values (for sand mould with a chill) are used in the present calculation. Calculations were also extended to a finer microstructure found in castings produced using high pressure die casting (HPDC) (Ref 20).

The moving distance of β/α interface, i.e. $(X_t - X_0)$, after annealing for a period of time t, can be obtained from Eq 2. Then, the fraction of undissolved $\beta_{\text{-eut}}$ plate can be calculated:

$$f_{\beta\ \text{undissolved}} = f_{\beta\ \text{as-cast}} \times \left(\frac{S_{\beta\ \text{as-cast}} - S_\beta}{S_{\beta\ \text{as-cast}}}\right) \quad \text{(Eq 3)}$$

where f_β is the fraction of $\beta_{\text{-eut}}$ phase. $S_{\beta\ \text{as-cast}}$ is the initial thickness of $\beta_{\text{-eut}}$ plate, and $S_\beta = 2 \times (X_t - X_0)$ (see Fig. 2) is thickness of $\beta_{\text{-eut}}$ plate at time t.

$C_\alpha(x,t)$ was obtained by solving the 1-D Fick's 2nd diffusion equation:

$$\frac{\partial C_\alpha(x,t)}{\partial t} = D\frac{\partial^2 C_\alpha(x,t)}{\partial x^2} \quad \text{(Eq 4)}$$

using finite difference method. The right-hand side of Eq 4 was approximated using Crank-Nicholson (Ref 22) finite difference equation:

$$D\left(\frac{\partial^2 C_\alpha(x,t)}{\partial x^2}\right)_{i,j} \approx \frac{D}{2}\left\{\begin{array}{l}\frac{1}{(\Delta x)^2}\left(C_\alpha(i-1,j) - 2C_\alpha(i,j) + C_\alpha(i+1,j)\right) + \\ \frac{1}{(\Delta x)^2}\left(C_\alpha(i-1,j+1) - 2C_\alpha(i,j+1) + C_\alpha(i+1,j+1)\right)\end{array}\right\} \quad \text{(Eq 5)}$$

The left-hand side of Eq 4 was approximated by a central difference of time step Δt:

$$\frac{\partial C_\alpha(x,t)}{\partial t} \approx \frac{1}{\Delta t}\left(C_\alpha(i,j+1) - C_\alpha(i,j)\right) \quad \text{(Eq 6)}$$

Al distributions in as-cast state were used as the initial condition. However, a corrected distribution is needed for the use as the initial condition. This was because when an electron beam hits the sample, it interacts with a certain volume of alloy. The exact α/β interface could not be established using EDS scan analysis. Hence, the position corresponding to the steepest concentration gradient was assumed as the β/α interface (Fig. 3). An accelerating voltage of 20 kV was used during EDS line scans. The interacting volume was ~2 μm in diameter. Thus, the measured EDS data at region 1 μm away from the assumed β/α interface, as indicated in Fig. 3, should not have been affected by the interaction volume and were therefore correctly measured.

In order to define the initial condition properly for numerical calculation through best data fitting, the "Five Parameter

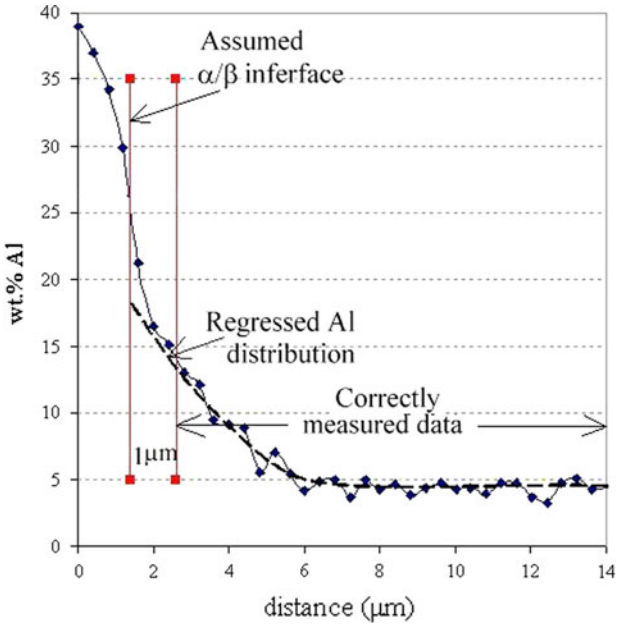

Fig. 3 A schematic showing the determined α/β interface based on the measured data of composition, the correctly measured data in region starting 1 μm away from the determined α/β interface, and the extrapolation of regressed Al content to the determined α/β interface (dash line)

Sigmoid" regression equation (Eq 7) was applied to treat the data obtained by EDS line scanning.

$$C_\alpha(x,0) = C_0 + \frac{a}{[1+e^{-(x/b)}]^c} \quad \text{(Eq 7)}$$

where C_α is the regressed Al concentration at location x (the distance from the β/α interface). C_0, a, b, and c are constants. C_α within 1 μm from the β/α interface was obtained by the extrapolation of the regressed one from outside 1 μm to the assumed β/α interface following Eq 7, as shown by the dashed line in Fig. 3. This regressed and extrapolated Al distribution is named as the corrected initial Al distribution for numerical calculation.

Al diffusivity (D_{Al}) in α(Mg) matrix, as determined by Moreau et al. (Ref 23), was used in the present calculation:

$$D = 1.2 \times 10^{-3} \exp\left(-\frac{143,449}{RT}\right) \frac{m^2}{s} \quad \text{(Eq 8)}$$

where R is the gas constant and T is the temperature. Equation 8 accounts for the combination of both lattice and grain boundary diffusion, although dissolution process is lattice diffusion dominant.

4. Results and Discussion

4.1 Initial As-Cast β Phase

EBSD quantitative analyses were conducted on cast samples taken from riser end and chill end locations, each of which experienced an extreme (lowest and highest) cooling rate during casting. f_β was determined, on an average of measurements made on two samples for each location, to be 11.2 and 12.3% for the riser and chill end samples, respectively. These values agree well with the results reported recently by Yakubtsov et al. (Ref 7) on an AZ81 cast alloy to be 10.2% for non-grain refined and 11.8% for grain refined cast samples. Their measurements were based on quantitative metallography using SEM images. Our values and those from Yakubtsov et al. (Ref 7) both show a slight increase of β phase with a finer microstructure. A slightly overall higher f_β in our case is due to the higher Al content in AZ91 cast alloy than that in AZ80 alloy used by Yakubtsov et al. (Ref 7).

β phase in AZ91 cast alloy exhibits two morphologies, as shown in Fig. 1. The irregular eutectic $\beta_{\text{-eut}}$ phase formed during the last stage of solidification, and lamellar discontinuous β precipitates formed during cooling in solid state after the end of solidification (Ref 24). The very high resolution of EBSD approach enables the area measurement of discontinuous β precipitates, and gives a total f_β including both discontinuous and eutectic β phase. The submicron discontinuous β precipitates, as is indicative in Fig. 1, should dissolve quickly when a sample is exposed to the annealing temperature as the reverse of the discontinuous precipitation process. Hence, homogenization process of AZ91 cast alloy is dominated by the dissolution of $\beta_{\text{-eut}}$ phase. Thus, "ImageJ" software was used to measure $f_{\beta\text{-eut}}$ on digital metallographic images.

4.2 Features of Dissolving $\beta_{\text{-eut}}$ and Al Distribution

Figure 4 shows the features of the plate-like $\beta_{\text{-eut}}$ connected particles in a sample in the as-cast state and after 30 min annealing. Considerable thinning of $\beta_{\text{-eut}}$ particle can clearly be

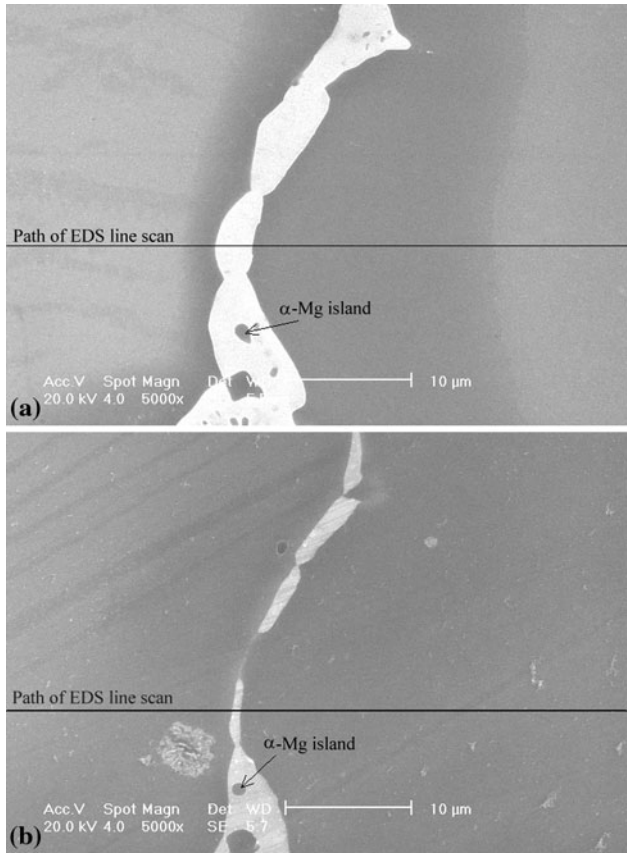

Fig. 4 SEM images showing the morphology of a $\beta_{\text{-eut}}$ particle in a riser end cast sample: (a) in the as-cast state and (b) after 60 min annealing at 420 °C. EDS scan lines are shown

seen after annealing. EDS data of Al contents in α(Mg) phase along the lines indicated in Fig. 4 are plotted in Fig. 5, together with the corrected Al distribution curves. Note that a distance being zero in Fig. 5 represents the location of α(Mg) at β/α interface. As shown in Fig. 5, the concentration gradient of Al content on the right-hand side of $\beta_{\text{-eut}}$ particle is considerably lower than the one on the left in the as-cast state. This corresponds well to the appearance in Fig. 4 where the darker eutectic α(Mg) is significantly wider than the one on the left. Annealing has led to a more symmetrical Al distribution.

It is clear from the EDS data that Al content in α(Mg) toward the interface is ~15% in the as-cast state, significantly higher than the maximum solubility predicted in the equilibrium Mg-Al phase diagram. This is reasonable as the non-equilibrium solidification, particularly associated with a divorced eutectic solidification, has resulted in the growth of α(Mg) with the Al content well beyond the solubility limit. The non-equilibrium solidus and liquidus extended below the eutectic temperature is depicted in Fig. 6. Thus, eutectic α(Mg) with supersaturated Al content (higher than maximum soluble Al content in the equilibrium α(Mg) phase at T_E) continued growing following the metastable solidus line of α(Mg). $\beta_{\text{-eut}}$ phase formed finally at T_β (Fig. 6) when the interdendritic liquid was sufficiently undercooled to a temperature well below the equilibrium T_E (Ref 25).

It is reasonable to assume that local equilibrium at the β/α interface establishes when a cast sample was reheated to the annealing temperature. EDS data for the 30 min annealed

sample in Fig. 5 show this effect. The corrected interface Al content of ~11% is close to the value of 10.5% from the equilibrium phase diagram. For this reason, "C_{max}" at annealing temperature is taken as C_α^* for $t > 0$ for the computation. Figure 7 shows the calculated Al concentration profiles for the chill and riser end samples annealed for different periods of time at 400 and 420 °C. SDAS at the chill location of the cast plate is 20 μm. For a clearer comparison, concentration data are only given up to 10 μm for both the chill and riser end samples. A higher diffusion rate at the higher annealing temperature is apparent for both samples.

As the Al distribution can be revealed for any annealing time, the simulation results in Fig. 7(a) and (c) have revealed an increasing and then decreasing Al concentration as a function

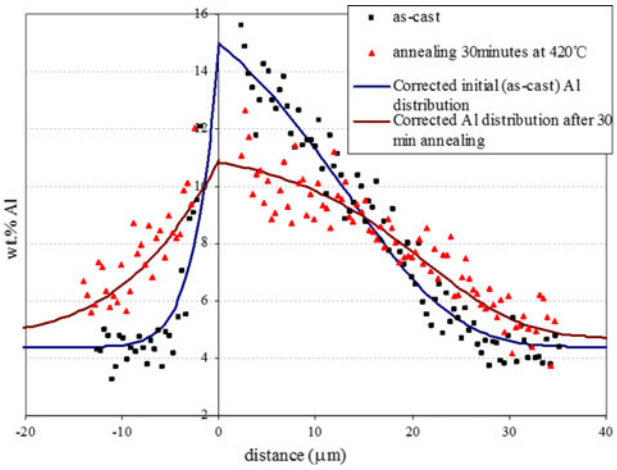

Fig. 5 Experimentally determined Al distributions (scatter points) and corrected (solid lines) Al distributions in the as-cast state and after 30 min annealing at 420 °C across α(Mg) phase in a riser end cast sample

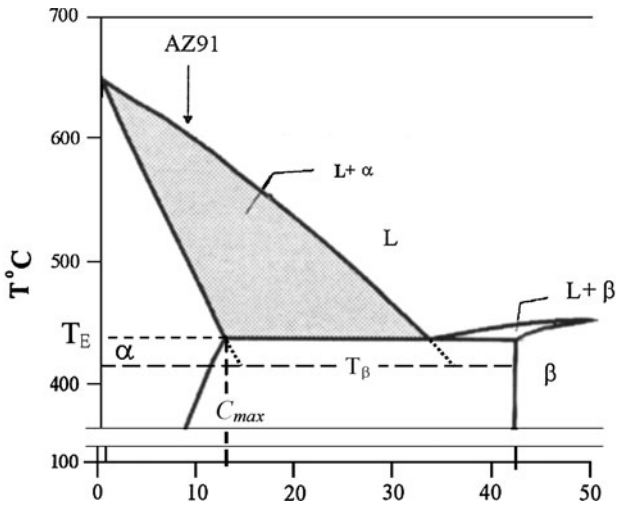

Fig. 6 Equilibrium Mg-Al phase diagram and the suggested metastable solidus and liquidus of α(Mg) phase

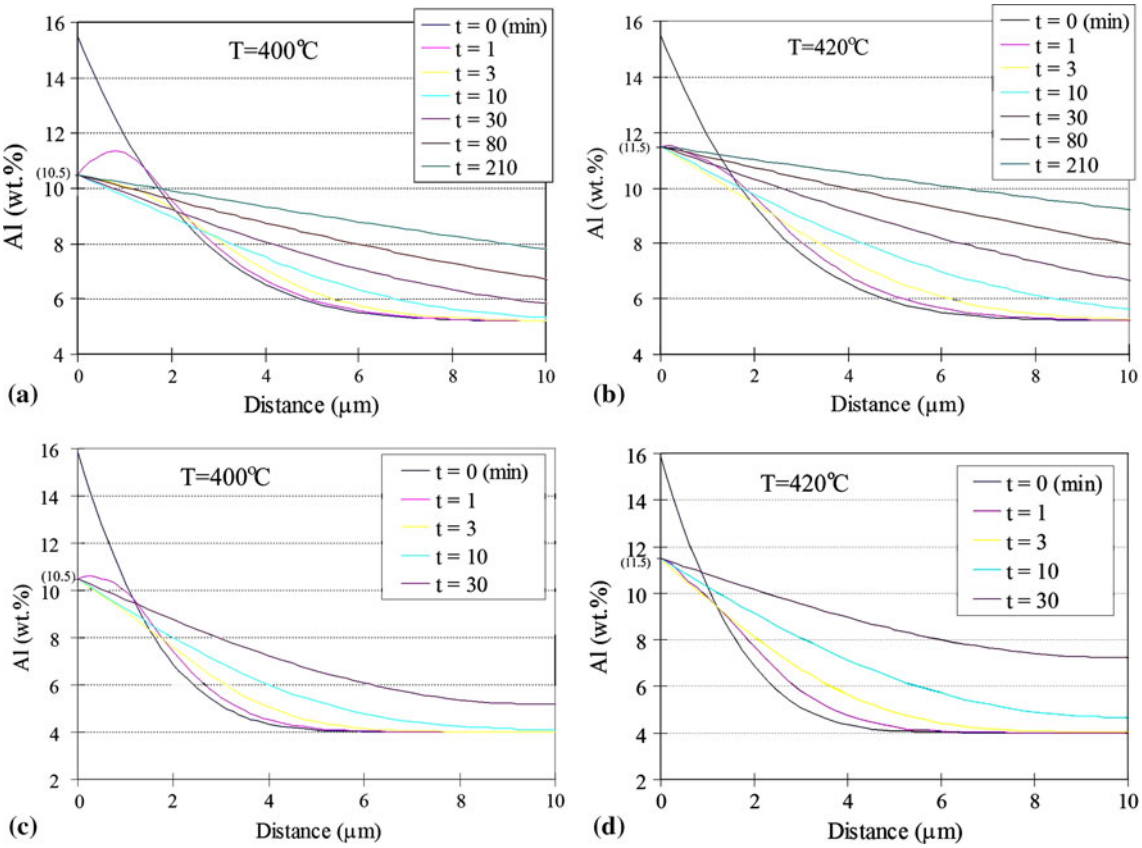

Fig. 7 Calculated Al distributions in α(Al) in the riser end location (a, b), and in the chill end location (c, d) after annealing for various periods of time, at 400 and 420 °C, respectively

of distance from the interface for a short annealing time of 1 min at 400 °C. For the data of 420 °C annealing, this occurred well within a minute. This concentration feature is the result of a non-equilibrium Al content in the as-cast state suddenly reduced to the equilibrium one as soon as annealing starts. This also means that in the front of interface there is a distance where Al content is higher than the equilibrium solubility limit. The "supersaturated" Al might, then, result in the growth of β particles, meaning that a slight increase in f_β occurs within a short period of time. The growth of β phase will end when the reverse Al concentration gradient has become flattened and the dissolution of $\beta_{\text{-eut}}$ phase proceeded afterwards.

4.3 Dissolution Rates of $\beta_{\text{-eut}}$ Phase

Experimental and calculated fractions of $\beta_{\text{-eut}}$ phase as a function of time in the three location specific cast samples are plotted in Fig. 8. The parameters required for the computation are summarized in Table 1, and the initial conditions (measured EDS data and corrected Al distributions in the as-cast state) are shown in Fig. 9. It can be seen in Table 1 that f_β in the as-cast samples decreased from riser end to chill end. In the present study, we have not attempted to further explain this trend of decrease in f_β. Eskin et al. reviewed the literature data regarding the effect of cooling rate on fraction of eutectics (f_E) in Cu alloys and showed some controversial tendencies of f_E when cooling rate was increased (Ref 26).

Figure 8 shows that the time required to dissolve $\beta_{\text{-eut}}$ to the minimum level is both temperature and as-cast microstructure (mainly the size of $\beta_{\text{-eut}}$) dependent. Figure 10 is an example clearly showing the decreasing amount of $\beta_{\text{-eut}}$ phase as the annealing time increases. Despite the simplification made for the theoretical computation as described before, it is clear from

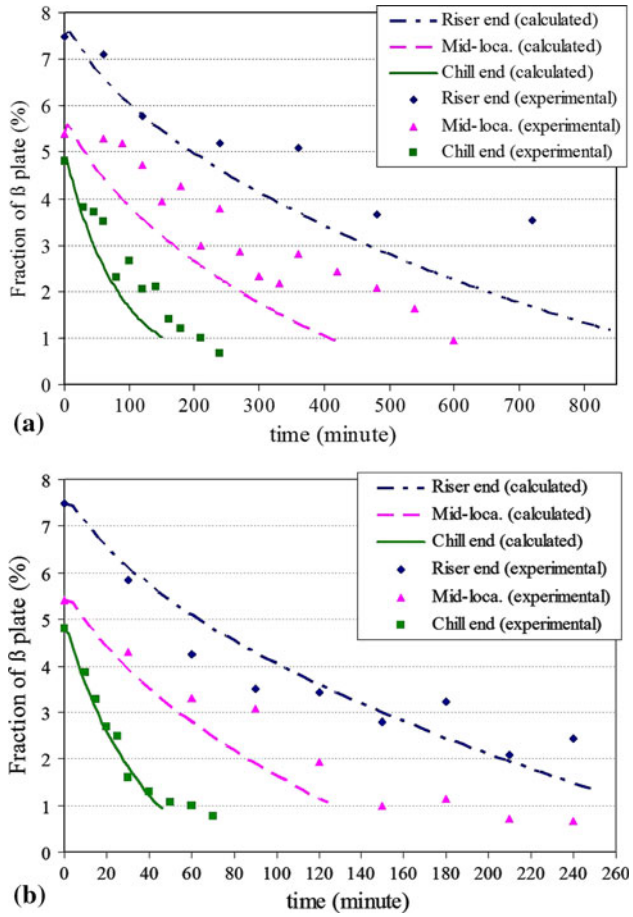

Fig. 8 Calculated and experimental results showing dissolution (reduction) of $\beta_{\text{-eut}}$ phase as a function of time in three location specific samples during annealing at (a) 400 °C and (b) 420 °C

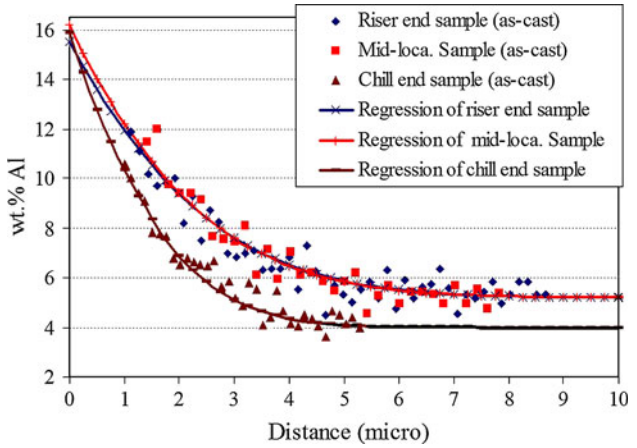

Fig. 9 Al distributions regressed and extrapolated to β/α interface (at location with 0 distance) from EDS results measured in the as-cast samples

Table 1 Parameters for the calculation of solid dissolution of plate-like $\beta_{\text{-eut}}$ phase

Sample type location	Diffusion domain, μm (a)	Initial f_β, %	C^*_α, wt.% Al (b)		ρ_β, g/cm^3 (c)	ρ^*_α, g/cm^3 (c)	ρ_α, g/cm^3 (c)	Thickness of β plate, μm (d)
			400 °C	420 °C				
Cast-riser (e)	32	7.5	10.5	11.5	2.13	1.84	1.78	5.8
Cast-mid (e)	23	5.4	10.5	11.5	2.13	1.84	1.78	3.8
Cast-chill (e)	10	4.8	10.5	11.5	2.13	1.84	1.78	2.6
HPDC (f)	5	4.8	10.5	11.5	2.13	1.84	1.78	1.0

(a) Diffusion domain equals to a half of dendrite arm space
(b) C^*_α is the equilibrium concentration of α(Mg) phase at α/β interface
(c) Phase density ≈ (wt.% Al) × density of pure Al + (wt.% Mg) × density of pure Mg
(d) Thickness of β plate equals to the average size of $\beta_{\text{-eut}}$ particles in the as-cast samples
(e) Casting samples from this work
(f) High-pressure die casting (HPDC) from Cáceres et al. (Ref 20) and the thickness of $\beta_{\text{-eut}}$ phase was measured based on a micrograph in Ref 20

Fig. 8 that the theoretically predicted fraction of β_{-eut} decreasing with time agreed reasonably well with the experimental data, particularly for the case at 420 °C (Fig. 8b), suggesting that the consideration based on diffusion and mass balance is correct.

The significance of the results in Fig. 8 is the relevance for the consideration of the liquation phenomenon during welding. It has been suggested (Ref 17) that the "critical heating rate" could not normally be obtained in a practical welding process due to the slow dissolution rate of β_{-eut} phase. This has now been fully confirmed by the present experimental and computed results. Taking the chill end sample for example, the presented results in Fig. 8(b) suggested that more than 50 min are required to dissolve the majority of β_{-eut} at 420 °C, which is very close to the lowest temperature of partial melting at ~424 °C (Ref 25, 27). The data also show that it takes ~10 min for a 10% reduction in f_β from the original value in the cast state. We further recognize that $(df_\beta/dt)_{25 \rightarrow 420\ ^\circ C} \ll (df_\beta/dt)_{420\ ^\circ C}$ and it only takes ≪10 s to reach ~424 °C during the up-heating stage of most welding processes. Hence, it can be concluded that the reduction of f_β is insignificant during the up-heating stage of welding to affect the degree of partial melting. Similar reasoning can be applied to cast samples taken from the riser end location and from the mid-location of the plate.

With regards to the dissolution heat treatment of cast AZ91 alloy, Fig. 8 provides a guideline for the treatment practice to reduce the amount of β_{-eut} in the normal gravity sand and metal mould AZ91 alloy castings. It is clear that the required time for dissolution of β_{-eut} strongly depends on the cooling rate during solidification. This solidification condition determines the initial amount and size of β_{-eut} in the cast state. A lower cooling rate during solidification results in a higher amount and coarser β_{-eut} and hence requires a longer time to reduce β_{-eut} to the same amount. For the normally thick sand castings, the required treating time for an almost complete dissolution of β_{-eut} could be several hours. On the other hand, castings produced using a metal mould may just need about an hour to almost completely dissolve β_{-eut} phase.

Heat treatment may also be extended to high-pressure die casings because vacuum high-pressure die castings are heat treatable. The calculated results shown in Fig. 11 indicated that at 420 °C, a treating time of less than 10 min is sufficient for dissolution treatment of the castings. Recent results (Ref 28) have shown that, for aluminum alloys, a reduction of ~20 °C in the normal solution heat-treatment temperature can prevent blister formation in normal (non vacuum) high-pressure die castings. If this can be extended for magnesium high-pressure die castings, a dissolution treatment at 400 °C may be used without blister formation. The present dissolution analysis has suggested, as also shown in Fig. 11, a complete dissolution is possible well within an hour.

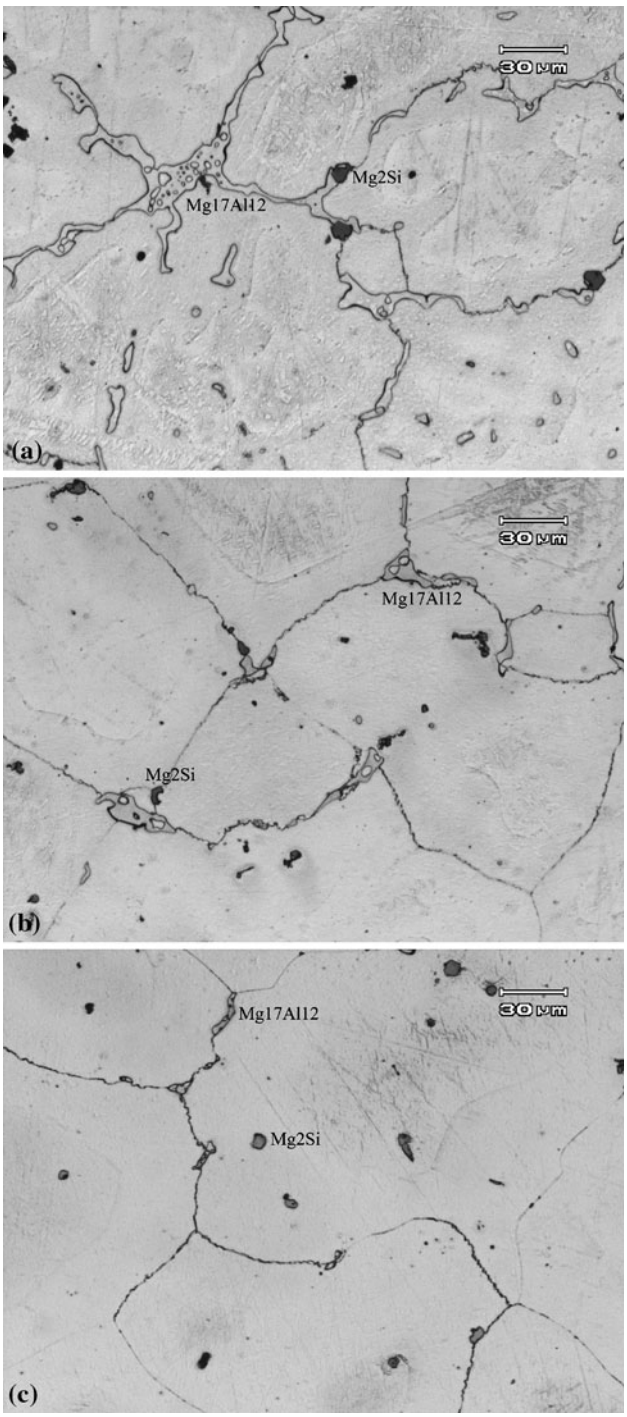

Fig. 10 Micrographs showing features due to the dissolution of β_{-eut} particles in mid-location samples annealed at 420 °C for: (a) 30 min, (b) 120 min, and (c) 240 min

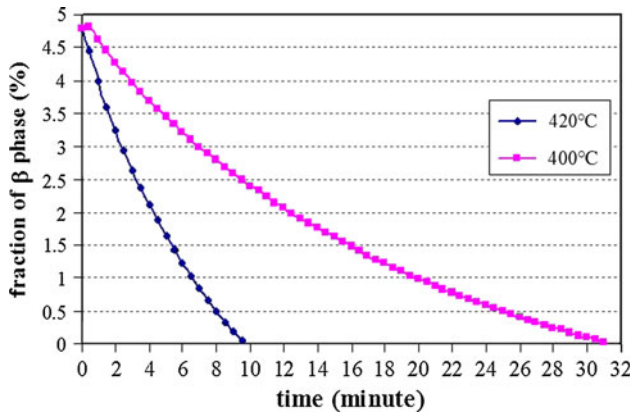

Fig. 11 Fraction of β phase in high-pressure die castings as a function of treating time during isothermal treating at 420 and 400 °C

5. Conclusions

Dissolution of β_{-eut} phase in AZ91 alloy at temperatures close to but below the incipient melting temperature was studied. The theoretically computed reduction in the amount of the phase as a function of time based on diffusion and mass balance agrees reasonably well with the experimental results. Hence, the kinetics of β_{-eut} dissolution is basically diffusion controlled. The present experimental and computational results suggest that for best dissolution treatment practice, heat-treating condition should be set according to the size of cast microstructure. Although a few hours may be required for sand castings, an hour should be sufficient for metal mould castings. For the case of welding, it would take tens of minutes, depending on the original microstructure of the alloy, for a 10% reduction in the amount of β_{-eut} even at 420 °C which is very close to the incipient melting temperature. Hence, due to the up heating time of less than 10 s to the incipient melting temperature during welding, there is practically no ''critical heating rate'' to affect the inevitable partial melting process to a significant extent.

References

1. J.F. King, Magnesium: Commodity or Exotic? *Mater. Sci. Technol.*, 2007, **23**(1), p 1–14
2. L.A. Dobrzanski, T. Tanski, L. Cízek, and Z. Brytan, Structure and Properties of Magnesium Cast Alloys, *J. Mater. Process. Technol.*, 2007, **192–193**, p 567–574
3. T.P. Zhu, Z.W. Chen, and W. Gao, Effects of Microstructure and Partial Melting on Tensile Properties of AZ91 Magnesium Cast Alloy, *Mater. Sci. Forum*, 2007, **546–549**, p 65–68
4. X. Du and E. Zhang, Microstructure and Mechanical Behaviour of Semi-Solid Die-Casting AZ91D Magnesium Alloy, *Mater. Lett.*, 2007, **61**(11–12), p 2333–2337
5. S. Lun Sin, D. Dubé, and R. Tremblay, An Investigation on Microstructural and Mechanical Properties of Solid Mould Investment Casting of AZ91D Magnesium Alloy, *Mater. Charact.*, 2008, **59**(2), p 178–187
6. H.T. Kang and T. Ostrom, Mechanical Behavior of Cast and Forged Magnesium Alloys and Their Microstructures, *Mater. Sci. Eng. A*, 2008, **490**(1–2), p 52–56
7. I.A. Yakubtsov, B.J. Diak, C.A. Sager, B. Bhattacharya, W.D. MacDonald, and M. Niewczas, Effects of Heat Treatment on Microstructure and Tensile Deformation of Mg AZ80 Alloy at Room Temperature, *Mater. Sci. Eng. A*, 2008, **496**(1–2), p 247–255
8. Y.Z. Lü, Q.D. Wang, W.J. Ding, X.Q. Zeng, and Y.P. Zhu, Fracture Behavior of AZ91 Magnesium Alloy, *Mater. Lett.*, 2000, **44**(5), p 265–268
9. S. Kleiner, O. Beffort, A. Wahlen, and P.J. Uggowitzer, Microstructure and Mechanical Properties of Squeeze Cast and Semi-Solid Cast Mg–Al Alloys, *J. Light Met.*, 2002, **2**(4), p 277–280
10. M.M. Avedesian and H. Baker, *Magnesium and Magnesium Alloys*, ASM International, 1999, p 79
11. A. Stern and A. Munitz, Partially Melted Zone Microstructural Characterization from Gas Tungsten-Arc Bead on Plate Welds of Magnesium AZ91 Alloy, *J. Mater. Sci. Lett.*, 1999, **18**(11), p 853–855
12. M. Marya and G.R. Edwards, The Laser Welding of Magnesium Alloy AZ91, *Weld. World*, 2000, **44**(2), p 31–37
13. A. Munitz, C. Cotler, A. Stern, and G. Kohn, Mechanical Properties and Microstructure of Gas Tungsten Arc Welded Magnesium AZ91D Plates, *Mater. Sci. Eng. A*, 2001, **302**(1), p 68–73
14. M. Marya and G.R. Edwards, Influence of Laser Beam Variables on AZ91D Weld Fusion Zone Microstructure, *Sci. Tech. Weld. Join.*, 2002, **7**(5), p 286–293
15. M. Marya, G.R. Edwards, and S. Liu, An Investigation on the Effects of Gases in GTA Welding of a Wrought AZ80 Magnesium Alloy, *Weld. J.*, 2004, **83**(7), p 203s–212s
16. X. Cao, M. Xiao, M. Jahazi, and J.P. Immarigeon, Continuous Wave ND:YAG Laser Welding of Sand-Cast ZE41A-T5 Magnesium Alloys, *Mater. Manuf. Process.*, 2005, **20**(6), p 987–1004
17. T.P. Zhu, Z.W. Chen, and W. Gao, Incipient Melting in Partially Melted Zone During Arc Welding of AZ91D Magnesium Alloy, *Mater. Sci. Eng. A*, 2006, **416**(1–2), p 246–252
18. Z.D. Zhang, L.M. Liu, Y. Shen, and L. Wang, Mechanical Properties and Microstructures of a Magnesium Alloy Gas Tungsten Arc Welded with a Cadmium Chloride Flux, *Mater. Charact.*, 2008, **59**(1), p 40–46
19. S. Kou, *Welding Metallurgy*, 2nd ed., Wiley, New York, 2002, p 321–329
20. C.H. Cáceres, W.J. Poole, A.L. Bowles, and C.J. Davidson, Section Thickness, Macrohardness and Yield Strength in High-Pressure Diecast Magnesium Alloy AZ91, *Mater. Sci. Eng. A*, 2005, **402**(1–2), p 269–277
21. C.H. Cáceres, C.J. Davidson, J.R. Griffiths, and C.L. Newton, Effects of Solidification Rate and Ageing on the Microstructure and Mechanical Properties of AZ91 Alloy, *Mater. Sci. Eng. A*, 2002, **325**(1–2), p 344–355
22. K.A. Hoffmann and S.T. Chiang, *Computational Fluid Dynamics*, Vol 1, 4th ed., Engineering Education System, Wichita, Kan, 2000, p 63–67
23. G. Moreau, J.A. Cornet, and D. Calais, Acceleration de la diffusion chimique sous irradiation dans le systeme aluminium-magnesium, *J. Nucl. Mater*, 1971, **38**(2), p 197–202 (in French)
24. A.K. Dahle, Y.C. Lee, M.D. Nave, P.L. Schaffer, and D.H. St John, Development of the As-Cast Microstructure in Magnesium–Aluminium Alloys, *J. Light Met.*, 2001, **1**(1), p 61–72
25. Y. Wang, B. Sun, Q. Wang, Y. Zhu, and W. Ding, An Understanding of the Hot Tearing Mechanism in AZ91 Magnesium Alloy, *Mater. Lett.*, 2002, **53**(12), p 35–39
26. D. Eskin, Q. Du, D. Ruvalcaba, and L. Katgerman, Experimental Study of Structure Formation in Binary Al-Cu Alloys at Different Cooling Rates, *Mater. Sci. Eng. A*, 2005, **405**(1–2), p 1–10
27. M. Ohno, D. Mirkovic, and R. Schmid-Fetzer, Liquidus and Solidus Temperatures of Mg-Rich Mg-Al-Mn-Zn Alloys, *Acta Mater.*, 2006, **54**(15), p 3883–3891
28. R.N. Lumley, R.G. Odonnell, D.R. Gunasegaram, and M. Givord, Heat Treatment of High-Pressure Die Castings, *Metall. Mater. Trans. A*, 2007, **38A**(10), p 2564–2574